nature communications

Article

https://doi.org/10.1038/s41467-026-75094-6

Ultra flash cold events under global warming

Received: 9 January 2026

Accepted: 23 June 2026

Published online: 02 July 2026

Check for updates

Yongli He[1,2], Zhanbo Wang[1], Xiaodan Guan[1,2] ✉, Yongkun Xie[2] & Jianping Huang[2] ✉

It is widely assumed that global warming will make winters milder and reduce extreme cold. However, this assumption is contradicted by the recurrence of flash cold (FC) events—sudden, violent temperature drops that can freeze energy grids and infrastructure within hours. The 2021 North America freeze, which caused over $20 billion in losses, stands as a stark warning. Here, we find that while the world warms, the fate of these ultra FC events is diverging: they are fading over Eurasia but significantly intensifying over North America. By tracking the spatiotemporal evolution of these ultra FC events and characterizing their dynamic environment, we reveal that this contrast is driven by specific atmospheric circulation regimes. In North America, increasingly frequent Alaska–Arctic anticyclonic anomalies funnel cold air directly southward. Conversely, weakened Ural–Arctic cyclonic anomalies are cutting off the cold supply. Crucially, current climate models fail to reproduce this intercontinental divergence. Simulations largely miss these specific circulation regimes, leading models to underestimate the ultra FC risk. Our results expose a regional warming paradox: specific atmospheric circulation anomalies can transiently overwhelm background warming, creating a critical blind spot for energy security.

Accelerated greenhouse warming is reshaping not only the magnitude of climate extremes but also the speed at which they unfold. A growing class of flash hazards, spanning flash floods[1,2], flash droughts[3,4] and rapid temperature whiplashes[5–9], illustrates how abrupt transitions can rival traditional threshold-based extremes in their societal and ecological consequences. Extending this rate-dependent perspective to the cold sector, we focus on flash cold (FC) events, defined as sudden, violent temperature drops (defined here as the day-to-day difference in daily mean temperature). Unlike slow-onset cold spells, FC events constitute an overlooked subset of cold-air outbreaks capable of inflicting acute damage on vegetation[10], spiking respiratory mortality[11], and paralyzing energy supply[12]. Recent catastrophes underscore their disruptive potential: from the 2017 Balkan plunges[13] to the historic 2021 freeze in eastern China[14] and the record-breaking −78 °C windchill on Mount Washington in 2023[15], these events reveal a systemic volatility that persists despite a warming background.

Global warming has unequivocally reduced the frequency of absolute cold extremes[16,17], yet the recurrence of high-impact cold outbreaks creates a "warming paradox" that remains hotly debated[18–20]. Competing hypotheses attribute these events to Arctic amplification and increased waviness of polar vortex[21,22], shifts in blocking regimes[19,23–25] or internal variability[26,27]. However, resolving this debate is impeded by a fundamental methodological limitation: cold extremes are typically defined relative to a warming climatological baseline. As the baseline rises, traditional fixed-percentile or absolute-threshold indices are heavily damped, such that their capture of merely static severity inadvertently masks the risks rooted in enhanced dynamical variability. Consequently, a distinct class of events—those driven by intense circulation dynamics rather than absolute minima—may be intensifying outside the scope of conventional metrics.

To unmask these hidden risks, a shift from magnitude-based to rate-based diagnostics is essential. Although temperature-drop criteria exist in various operational cold-surge definitions, they generally evaluate accumulated cooling over extended multi-day windows (e.g., 48 to 72 h). In contrast, our FC framework strictly isolates the rate of cooling within a 24-h timescale, thereby capturing the true flash nature of these abrupt synoptic shocks. Furthermore, recent studies have

[1]Key Laboratory for Semi-Arid Climate Change of the Ministry of Education, School of Atmospheric Sciences, Lanzhou University, Lanzhou, Gansu, China. [2]Collaborative Innovation Center for Western Ecological Safety, Lanzhou, China. ✉e-mail: guanxd@lzu.edu.cn; hjp@lzu.edu.cn

begun to decouple event detection from warming background by focusing on rapid temperature change rates[7,28–30], revealing that sharp temperature drops have remained stable or even increased in regions where total cold days are declining[8,9,28]. However, diagnosing the full lifecycle of these events requires moving beyond isolated grid-point statistics. Synoptic cold surges evolve as continuous, mobile 3D structures in longitude-latitude-time space. Traditional grid-point approaches fracture these coherent systems, losing critical information regarding their propagation pathways and spatial extent. To overcome this, we employ a three-dimensional connected-component (3D-connected) algorithm, a framework successfully applied to droughts[31,32], heatwaves[33,34] and extreme colds[35]. By treating each cold spell as a coherent physical entity, this approach allows us to rigorously quantify the changing geometry and intensity of rapid cooling events in a warming world.

Here, we identify FC events across the Northern Hemisphere (1959–2021) and reveal a striking intercontinental divergence in their evolution. We focus on the top decile—ultra FC events—as proxies for the most societally disruptive outbreaks. By integrating the 3D-connected detection and self-organizing maps (SOMs) of atmospheric circulation and CMIP6 historical simulations, we attribute observed trends to distinct circulation regimes and isolate sources of model uncertainty. Crucially, we show that while Eurasia sees a decline in FC intensity, North America faces an increasing threat driven by specific blocking patterns. Our findings highlight the primacy of dynamical volatility over thermodynamic warming in shaping extreme cold risks, providing a mechanistic explanation for their persistence and localized intensification under global warming.

Results

Intensification of FC events and asymmetric trends in ultra FC events

Using a 3D-connected algorithm (Methods), we identified 11,773 FC events across the Northern Hemisphere (NH) over 62 winters (1959–2021). These events are defined as contiguous spatiotemporal structures where the day-to-day temperature drop (ΔT) exceeds 1.5 standard deviations of the local distribution (Fig. 1a). Spatially, FC events occur most frequently between 40°–60°N, exhibiting greater extensive and intensity over land than ocean (Supplementary Fig. 1b). A representative event from winter 2020 illustrates this dynamical evolution: originating near Novaya Zemlya on 22 December, it propagated eastward across Eurasian as a coherent system before dissipating over the Western Pacific on 1 January (Fig. 1b).

Crucially, FC events are dynamically distinct from traditional extreme cold (EC) events. While EC events reflect the static severity of low temperatures, FC events capture the rapid rate of cooling, leading to fundamentally different occurrence behaviors (Supplementary Fig. 2; and Supplementary Note 1). This conceptual decoupling is manifested in their contrasting long-term trends: during 1959–2021, the frequency of FC events remained statistically stable, defying the marked decline observed in EC events (Supplementary Fig. 3a). This persistence aligns with the differential trends between absolute temperature (T2m) and ΔT (Supplementary Note 2 and Supplementary Figs. 3–5), suggesting that rapid cooling mechanisms remain active despite background warming.

Although the total frequency of FC events appears stable, a significant internal redistribution toward higher intensity is underway.

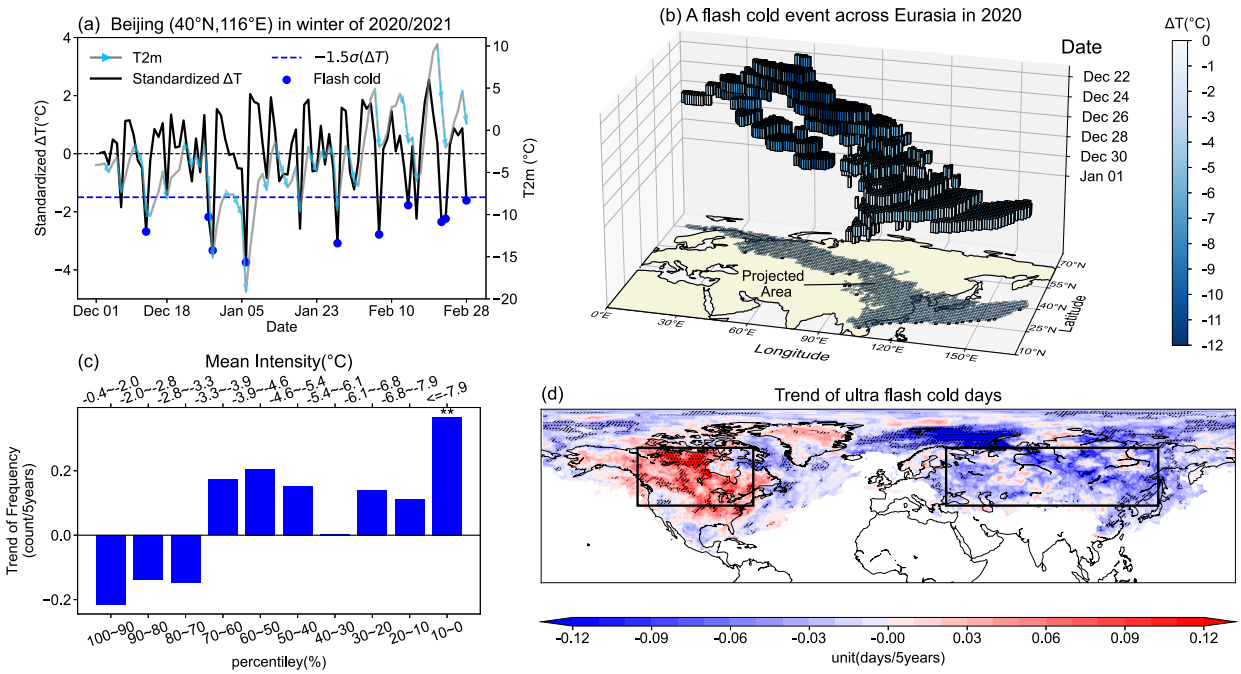


Fig. 1 | Identification and characteristics of flash cold (FC) events. a, **b** Example illustrating the identification of an FC event. **a** Time series of standardized 24-h temperature change (black solid line) and daily air temperature (gray solid line) in Beijing during winter 2020/2021. ΔT is defined as the 24-hour change in daily T2m ($T2m_t - T2m_{t-1}$). Light blue arrows mark individual 24-hour temperature drops. Grid points where ΔT <−1.5σ (blue dashed line) are flagged as potential FC occurrence. Blue circles denote time steps that satisfy the spatiotemporal connectivity criteria. **b** Spatiotemporal evolution of a contiguous FC event in 2020 identified by the 3D-connected algorithm. **c** Trends in the FC-event frequency as a function of mean intensity percentile (10% bins) over the Northern Hemisphere. Double asterisks denote significant trends at the 95% confidence level. **d** Spatial trends of ultra FC days (days per 5 years). Ultra FC days are counted strictly as grid/time instances belonging to the ultra FC events identified by the 3D-connected algorithm. Dots (hatches) indicate significance at the 95% (90%) confidence level. Black boxes represent the North America (40°–70°N, 70°–130°W) and Eurasia (40°–70°N, 30°–140°E) regions. The white areas over continents and oceans correspond to regions with no events or insufficient data.

https://doi.org/10.1038/s41467-026-75094-6

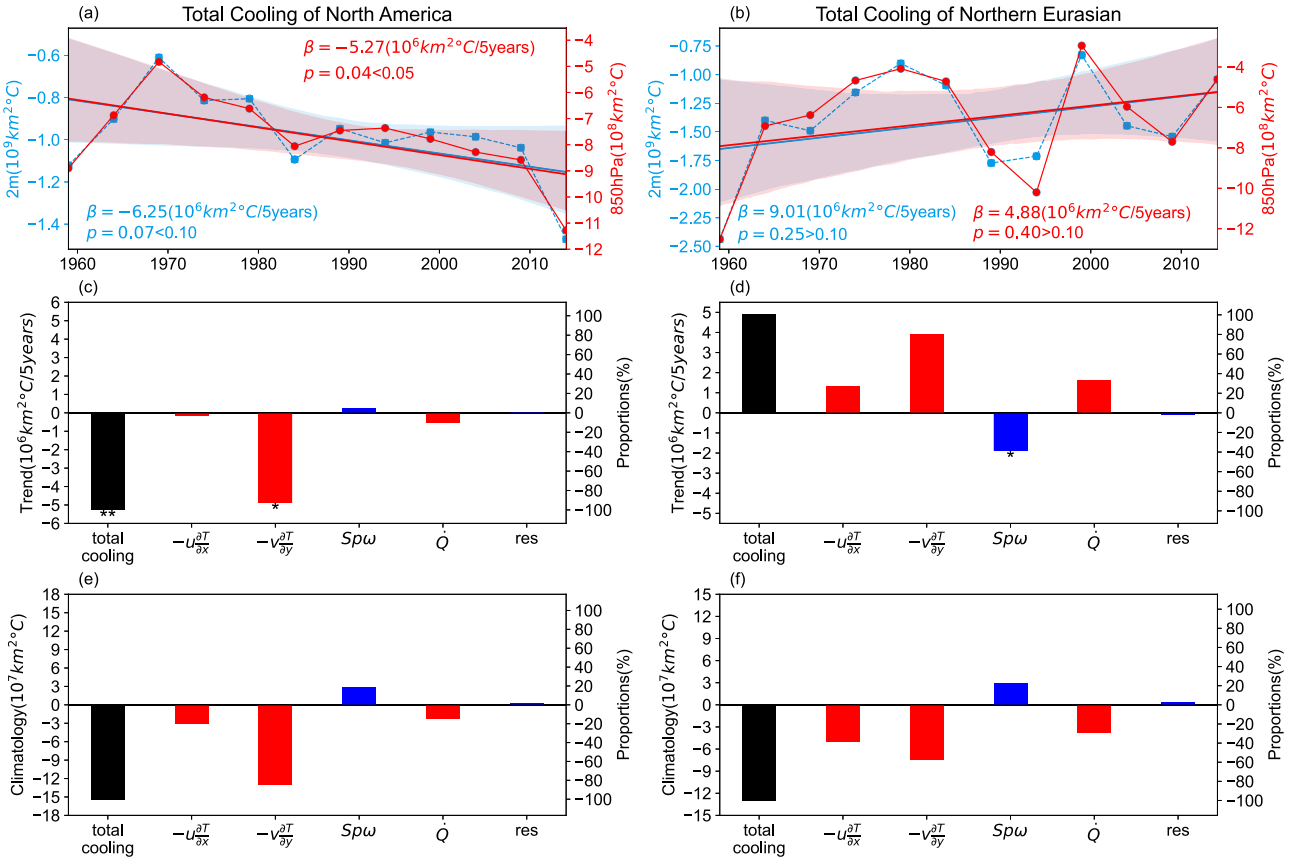


Fig. 2 | Contributions of temperature budget terms at 850 hPa. a, **b** Time series of total cooling at 2 m (light blue) and 850 hPa (red) over North America (**a**) and Eurasia (**b**). Linear trends are shown with straight lines, and shading denotes the 95% confidence interval. Trend slopes (β) and associated *p* values are indicated. **c**, **d** The relative contributions of individual physical processes to the trend of total cooling. Single (double) asterisk marks statistically significant trend at the 90% (95%) confidence level. **e**, **f** Same as (**c**, **d**), but for the contribution to climatology. In **c**–**f** red (blue) bars indicate the positive (negative) contributions to total cooling. The left panel corresponds to North America and right panel corresponds to Eurasia.

Mean FC intensity has strengthened significantly (Supplementary Fig. 3), driven by a shift in the event probability distribution (Fig. 1c). Specifically, we observe a decline in weaker FC events (70^{th}–100^{th} percentile, mean intensity > −3.3 °C) and a concurrent rise in stronger events (<−3.3 °C). The steepest increase is found in the most intense decile (0^{th}–10^{th} percentile, mean intensity <−7.9 °C), which is rising at a rate of 0.37 events per 5 years. Given their disproportionate societal impact, we define these top-decile events as "ultra FC events" and focus on their evolving spatial patterns.

Spatial analysis reveals two major activity centers for ultra FC days: North America (NA) and Eurasia (EA) (Supplementary Fig. 1d), yet their long-term trends exhibit a striking intercontinental asymmetry. Topographically, the Tibetan Plateau restricts southward cold-air penetration in EA, confining events north of 40°N; in contrast, the absence of such barriers in NA allows cold surges to propagate deeply into the continent. Most notably, area-weighted trends reveal a divergence (Fig. 1d): ultra FC days have significantly increased over NA (40°N–70°N, 70°W–130°W; +0.05 days per 5 years) while decreasing over EA (40°N–70°N, 30°E–140°E; −0.04 days per 5 years). Importantly, rigorous sensitivity testing demonstrates that these sharp regional contrasts are completely robust to non-stationary normalization methods (e.g., using de-trended ΔT or rolling baseline standard deviations; Supplementary Figs. 6 and 7). This confirms that distinct atmospheric circulation regimes, rather than uniform global warming, govern the evolution of ultra FC events on each continent.

To ensure our central finding of intercontinental divergence is robust to dataset choice, we cross-validated the trends using the independent NCEP reanalysis. Although the optimal statistical threshold for detecting the ultra FC events varies slightly due to inherent baseline differences between datasets, with the most pronounced intercontinental asymmetry appearing at the top 10% threshold in ERA5 and the top 20% threshold in NCEP (Supplementary Fig. 8), the fundamental physical pattern remains robust. Both datasets confirm that while Eurasian events are consistently decreasing, the frequency of ultra FC days over NA is experiencing a structural increase. Furthermore, restricting the analysis to these extreme upper percentile acts as a necessary spatial filter, which excludes abundant but meteorologically weaker maritime events, thereby unmasking the intensifying threat specifically over the continental landmasses.

Thermodynamic drivers of the intercontinental divergence

To unravel the physical mechanism driving the contrasting trends in ultra FC days, we diagnosed the temperature tendency budget derived from the thermodynamic equation. We calculated "total cooling" as the annual integration of temperature (ΔT) over all affected grid points (Methods). The aggregate cooling intensity exhibits a pronounced hemispheric contrast trend resembling the spatial pattern of frequency trends (Fig. 2a, b): it has significantly intensified (become more negative) by -6.25×10^6 km²•°C per 5 years over NA, while weakening (become less negative) by $+9.01 \times 10^6$ km²•°C per 5 years over EA. By decomposing this total cooling into four physical components: zonal and meridional temperature advection, and adiabatic/diabatic processes (Eqs. 5–6; residual negligible), we quantitatively attribute the origins of these divergent trends.

We focus on the 850-hPa level, which effectively captures the lower-tropospheric thermal dynamics of cold surges. Climatologically,

meridional temperature advection (cold-air transport from the north) serves as the dominant cooling engine on both continents (Fig. 2e, f). However, the role of diabatic processes differ substantially. Over NA, the ratio of meridional temperature advection to diabatic cooling is ~5.8, whereas over EA, it drops to ~2.0. This indicates that while NA events are primarily advection-driven, EA events are more sensitive to local diabatic processes (e.g., radiative cooling), consistent with previous trajectory-based studies[36,37]. In both regions, adiabatic heating acts as a damping term, offsetting the cooling induced by advection and radiation.

Decomposing the long-term trends reveals that the intercontinental divergence stems principally from opposing trends in the temperature advection (Fig. 2c, d). Over NA, the intensification of total cooling is dominated by a marked strengthening of cold meridional advection, which overwhelms negligible changes in other terms and points to a dynamic enhancement of northerly flow. In stark contrast, the weakening trend over EA is driven by the concurrent decline of both zonal and meridional temperature advection, accompanied by a decrease in adiabatic heating—a divergence from the increasing adiabatic heating observed over NA. Consequently, the trend components over NA amplify their climatological signs (i.e., cooling terms becoming colder), whereas over EA they act to weaken the climatological signal. This systematic contrast indicates that the observed asymmetry arises from opposite changes in cold advection processes associated with synoptic-scale circulation.

To reconcile the local grid-point trends (Fig. 1d) with the morphological properties of the 3D ultra FC events, it is essential to recognize that the 'total cooling' hazard is an integration of event intensity, frequency, duration, and area (Eq. 8 and Supplementary Table 1). Interestingly, the absolute frequency of 3D ultra FC events has increased over both continents (Supplementary Fig. 9). Therefore, the divergent local exposure is fundamentally driven by changes in event duration. Over Eurasia, the ultra FC events have become significantly shorter-lasting and smaller in extent, which overwhelmingly offsets the increased event frequency, resulting in a net decrease in local ultra FC days. Conversely, North America maintains longer-lasting events alongside the frequency increase, directly translating into heightened local exposure and elevated 'total cooling' risks. In the next section, we integrate these thermodynamic findings with circulation regimes to reveal the dynamical origins of this intercontinental divergence.

Atmospheric circulation regimes governing the asymmetric evolution of ultra FC trends

To elucidate the large-scale circulation governing the contrasting ultra FC trends, we classified recurrent circulation patterns using a self-organizing map (SOM) approach. This analysis identifies a set of circulation states that collectively account for >80% of all ultra FC days (Supplementary Table 2) and successfully reproduce the observed trends (Supplementary Fig. 10). Crucially, while individual SOM nodes are diverse, they dynamically cluster into two distinct archetypes whose divergent evolution explains the hemispheric contrast: the Alaska–Arctic anticyclonic regime (the driver of NA intensification) and the Ural–Arctic cyclonic regime (the driver of EA decline).

Over NA, the intensification of ultra FC days is dynamically anchored to the increasing frequency of the Alaska–Arctic anticyclonic Regime (patterns #4, #11, and #12; Fig. 3m–o). These patterns feature a robust upstream blocking over Alaska coupled with anticyclonic anomalies extending into the Arctic–a configuration that efficiently channels cold Arctic air southeastward into continent via a deep downstream trough. Under these conditions, meridional cold advection accounts for >70% of the cooling budget, overwhelming the relatively weak diabatic contribution (Fig. 3i–k). Consequently, this regime acts as a cold amplifier, significantly elevating ultra FC risk across midlatitude North America (Fig. 3e–g). In contrast, patterns featuring the Alaska–North Pacific trough (e.g., patterns #1, #2 and #9) confine cold air to high latitudes (Supplementary Fig. 11). Although some suppression patterns (e.g., #9) have declined, this is dynamically overridden by the surge in the Alaska–Arctic anticyclonic, yielding a net amplification of ultra FC days.

In stark contrast, the decline in ultra FC days over EA is primarily driven by the collapse of the Ural–Arctic cyclonic regime (pattern #9; Fig. 3p). This pattern, characterized by a deep trough over the Ural and a displaced Arctic cyclone, effectively serves as the primary highway for southward cold surges, exhibiting the strongest local risk enhancement (Supplementary Fig. 12g–i). Its marked weakening and reduced frequency dominate the hemispheric trend. While other patterns—such as Ural ridges directing flow from Novaya Zemlya (#11, #12) or cyclonic wave-breaking structures over the Okhotsk Sea (#2)—do facilitate some cold transport, their contributions are spatially limited or insufficient to offset the systematic retreat of the dominant Ural–Arctic cyclonic regime.

Beyond frequency shift, the asymmetry is reinforced by the divergent morphological evolution within the regimes themselves. Composites between the earlier and later 20-year periods reveal a double weakening for EA: the dominant Ural–Arctic cyclonic regime (#9) has not only become less frequent (Supplementary Fig. 13a) but also structurally weakened, with its cyclonic core shifting westward and amplitude dampening, thereby shrinking its daily impact area (Supplementary Fig. 13b, e). Conversely, NA exhibits structural resilience: the Alaska–Arctic anticyclonic regimes (#4/#11/#12) show only modest eastward displacements with no loss of intensity (Supplementary Fig. 13d). Consequently, the daily area influenced by these patterns remain stable (Supplementary Fig. 13b). The daily intensity of ultra FC events also remains stable across both continents (Supplementary Fig. 13c), indicating that the divergent trends are governed by the evolution of circulation frequency and spatial footprint, rather than changes in the localized magnitude of the events.

Taken together, these results demonstrate that the hemispheric asymmetry arises because the distinct circulation archetypes governing each continent are evolving in opposite directions. The Alaska–Arctic anticyclones—associated with enhanced blocking—have become more frequent and persistent, efficiently funneling cold air into NA. Conversely, the Ural–Arctic cyclones have weakened and become less frequent, constricting the primary cold-advection pathway into EA. These regime shifts are consistent with observed responses to global warming and sea-ice loss, including strengthened Arctic anticyclones[38], increased winter blockings/ridges over Alaska[39,40] and changes in Urals circulation[41,42]. Figure 3q presents a conceptual diagram summarizing how these divergent circulation archetypes modulate the asymmetric fate of ultra FC trends.

Inter-model uncertainty linked to circulation-regime biases

Given that the observed intercontinental divergence in ultra FC trends arises from specific circulation archetypes, the fidelity of future risk assessment hinges on the model's ability to reproduce these dynamical drivers. While CMIP6 models general capture the broad thermodynamic picture[29,30], their capability to simulate spatiotemporally coherent ultra FC events remains spatially inconsistent. Over NH, most models (18 of 24) correctly simulate an increased frequency of ultra FC events (Fig. 4a, top row), consistent with ERA5. However, substantial inter-model uncertainty obscures the regional signals. Over NA, the spread between the highest and lowest model climatology approaches one full day. Over EA, the ensemble systematically underestimates event frequency, consistent with previous studies[43]. Only three models (CNRM-CM6-1 ($p < 0.05$); EC-Earth3-Veg-LR and MRI-ESM2-0 ($p < 0.1$); Supplementary Fig. 14) successfully capture the pronounced continental contrast (i.e., increasing in NA vs. decreasing in EA). This disparity indicates that while models handle the global thermodynamic signal well, their representation of continental-scale dynamical trends remains deficient.

https://doi.org/10.1038/s41467-026-75094-6

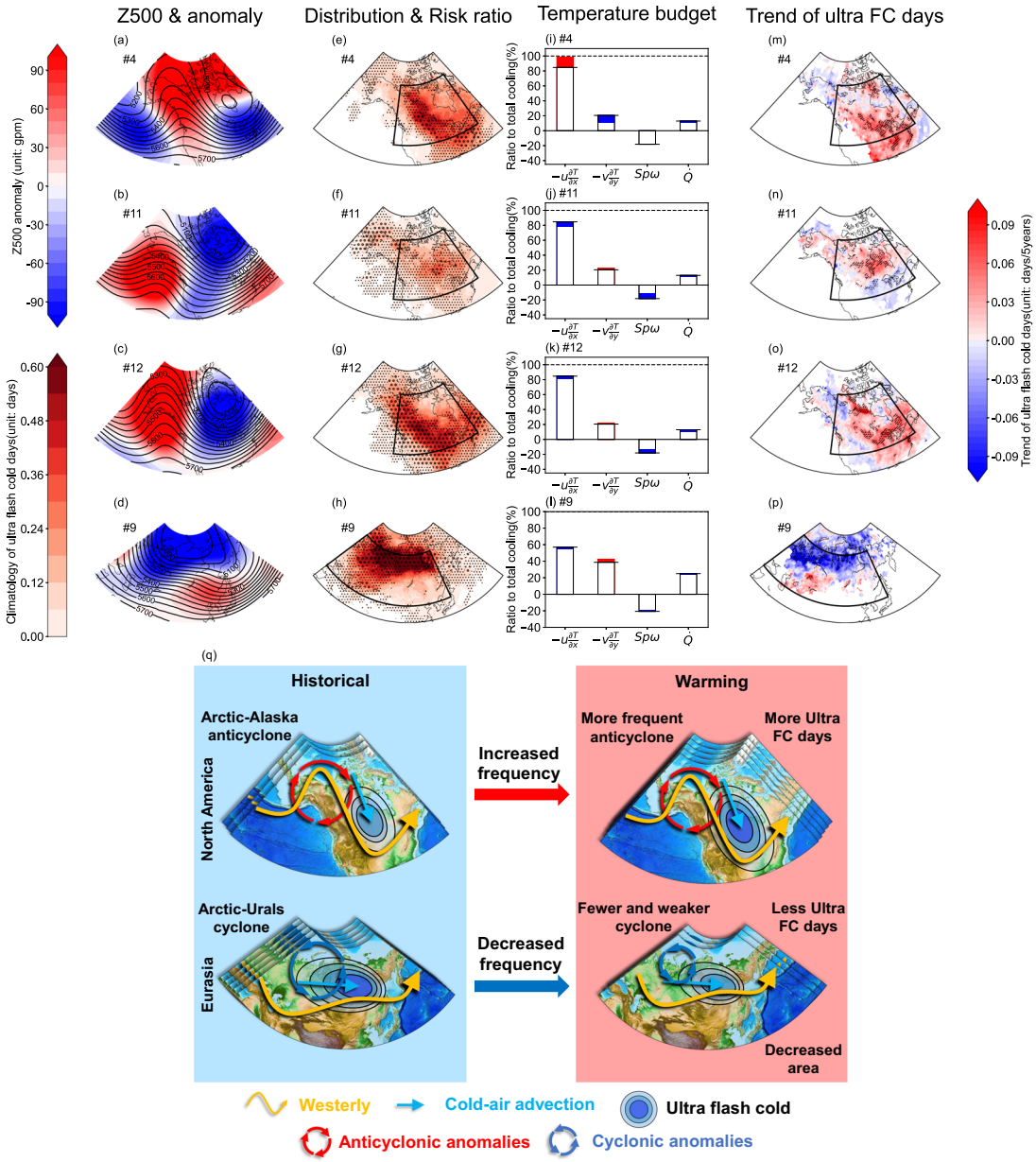


Fig. 3 | Circulation regimes and their thermodynamic characteristic associated with ultra flash cold (FC) events. The first three rows present dominant circulation patterns over North America (#4, #11, #12), and the bottom row displays the key pattern over Eurasia (#9). **a**–**d** Composites of 500-hPa geopotential height (contours) and anomalies (shading) for each circulation cluster. **e**–**h** Climatological distribution of ultra FC days associated with each pattern. Dots represent grid points where the risk ratios > 1, with coarse dots denote statistical significance at the 5% level based on the binomial test. **i**–**l** Relative contributions of each temperature budget terms to total cooling during ultra FC days. The columns represent the ratios of each term to total cooling, with the climatological mean denoted by a short horizontal line; red/blue shading denotes the magnitude above/below the mean. The residual term is negligibly small and has been omitted for clarity. **m**–**p** Pattern-specific contributions to the trend of ultra FC days, quantified by matching every ultra FC day to its concurrent circulation state. Dots (hatches) indicate significance at the 95% (90%) confidence level. **q** Schematic diagram illustrating the key spatial features and long-term changes of the dominant circulation systems over the two continents and their associated roles in modulating ultra FC events.

We trace the dominant source of this inter-model uncertainty to biases in simulating the key circulation regimes identified earlier. To isolate this link, we stratified the models into an "ERA5-similar" group (best performers) and an "ERA5-dissimilar" group (largest deviations) and compared their circulation fidelity (Fig. 4b–e). Over NA, the ERA5-similar group correctly simulates the increasing frequency of the Alaska–Arctic anticyclonic regimes, whereas the ERA5-dissimilar group erroneously simulates a decreasing trend, diametrically opposite to observations. Furthermore, regarding circulation intensity, the ERA5-similar group maintains changes near zero consistent with ERA5, while the ERA5-dissimilar group exhibits substantial biases. In contrast, over EA, the ERA5-similar group successfully reproduces the decreasing frequency of the Ural–Arctic cyclonic regime, although they underestimate the magnitude of this decline by roughly 50%. The ERA5-dissimilar group performs worse, showing weak or contradictory trends and failing to capture the geopotential height increases associated with the weakening cyclone.

https://doi.org/10.1038/s41467-026-75094-6

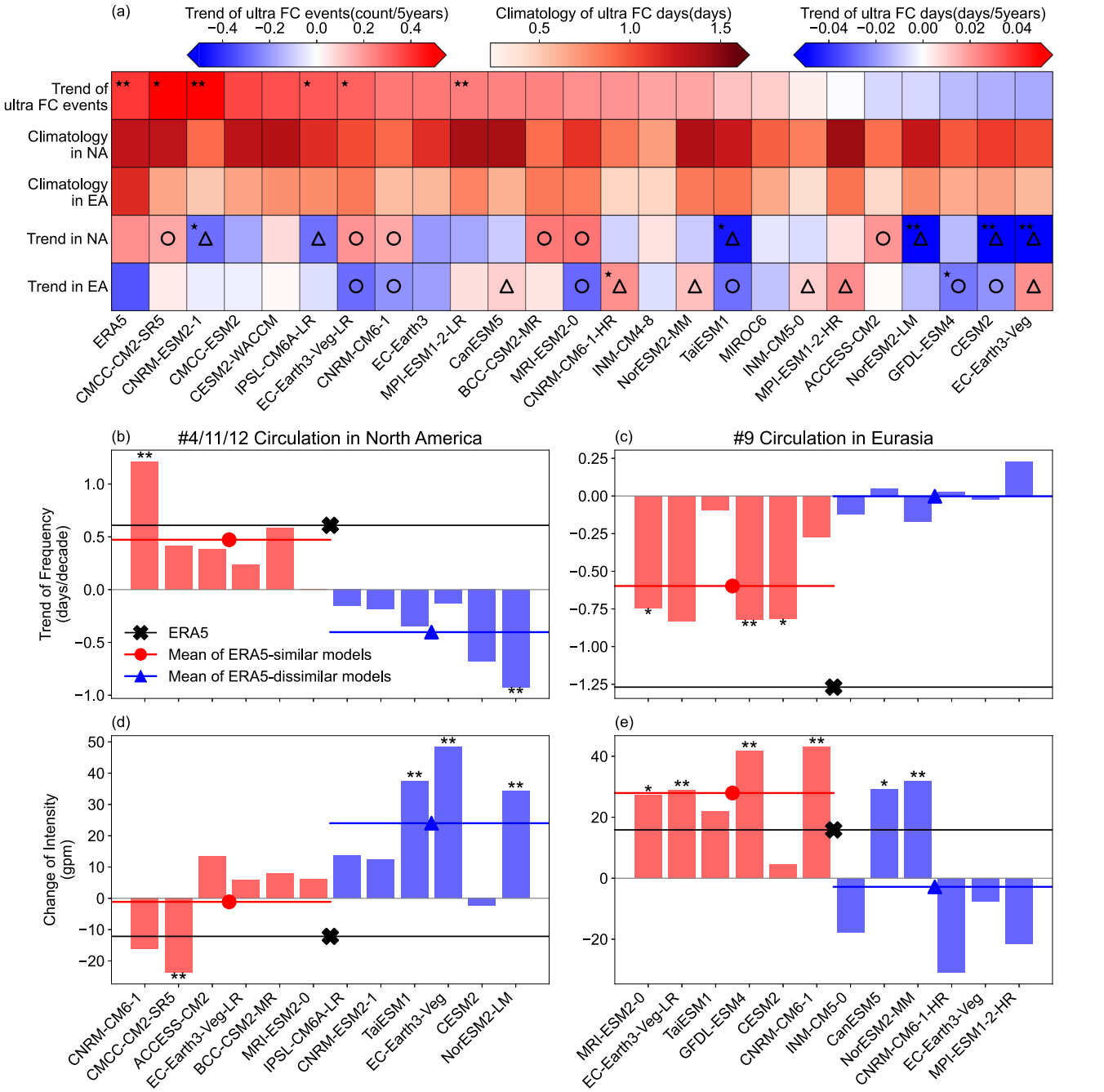


Fig. 4 | Evaluation of CMIP6 model performance in simulating ultra flash cold (FC) events and associated circulation-regime changes. a Trends of ultra FC event frequency, climatological ultra FC days, and their linear trend over North America (NA) and Eurasia (EA) for 24 CMIP6 historical simulations (1959–2014). Circles (triangles) highlight the six models whose trends of ultra FC days are most similar (dissimilar) to ERA5. **b**, **d** Trend in the frequency (**b**) and changes in the intensity (**d**) of the key circulation patterns over North America for ERA5, ERA5-similar models, and ERA5-dissimilar models. **c**, **e** Same as (**b**, **d**), but for Eurasia. Single (double) asterisk marks statistically significant trend at the 90% (95%) confidence level.

Collectively, the inter-model spread in ultra FC simulations is not mere stochastic noise, but is strongly coupled to the spread in their simulated regional circulation regimes, which likely stems from a combination of structural model biases and unforced internal climate variability. Specifically, the failure to capture the divergent frequency trends of the Alaska–Arctic and Ural–Arctic regimes prevent many models from reproducing the observed hemispheric asymmetry. This underscores that accurate simulation of sub-seasonal circulation dynamics—both in frequency and intensity—is a prerequisite for reliable projection of future flash cold risks.

Discussion

Our findings challenge the strictly thermodynamic assumption that global warming will uniformly mitigate cold extremes. While the frequency of threshold-defined cold events has indeed declined, our results demonstrate that FC events—characterized by rapid dynamical volatility—remain a persistent threat across the NH. By combining a rate-based diagnostic with a 3D-connected algorithm, we reveal that short-term temperature variability can intensify locally even as long-term climatological baselines rise. This decoupling suggests that the risks to ecosystems, infrastructure, and public health are not simply

vanishing with warming but are instead evolving from static severity to dynamical suddenness, preserving their potential for disruption.

A defining feature of this evolution is the pronounced hemispheric asymmetry in ultra FC trends, governed by distinct circulation-regime responses. We attribute the intensification over NA to the increasing frequency of Alaska–Arctic anticyclonic regimes, which reinforce blocking patterns over Alaska and amplify southwestward cold-air transport. In contrast, the decline over EA is mechanistically linked to the weakening and retreat of Ural–Arctic cyclonic regimes, which effectively constrict the primary northerly cold-advection pathway. These findings underscore that circulation dynamics, rather than mean background warming alone, act as the primary modulator of severe rapid cooling. Consequently, CMIP6 models that fail to capture these specific regime shifts are unable to reproduce the observed continental asymmetry, highlighting a critical bias in current projections of regional climate risk.

Beyond these dynamical biases, the general underestimation of ultra FC frequencies across CMIP6 models highlights inherent thermodynamic limitations. Coarse spatial resolutions numerically diffuse the sharp temperature gradients of propagating cold fronts, while stable boundary-layer parameterizations often produce excessive vertical mixing that overly damps near-surface day-to-day temperature variability. Therefore, while CMIP6 captures the dynamically-driven continental asymmetry, accurately projecting the absolute magnitude of future FC risks will necessitate high-resolution and convection-permitting modeling.

Our results also help reconcile an apparent tension in the literature regarding temperature variability. Previous studies have reported a multidecadal decline in intraseasonal temperature variability (ITV) across mid-to-high latitudes[44–47], a trend that seemingly contradicts the intensification of ultra FC events over NA reported here. We propose that this discrepancy arises from the sensitivity of diagnostics to temporal scales. Traditional variance metrics tend to smooth over short-lived, high-intensity fluctuations. By isolating the most rapid cooling episodes via ΔT-based diagnostics, we capture the sharp tail of the distribution that broad metrics may miss. Furthermore, to reconcile the strengthening cumulative cold advection over North America (Fig. 2) with the background weakening of the wintertime mean meridional temperature gradient driven by Arctic Amplification (Supplementary Fig. 15a), it is essential to distinguish between the climatological mean state and the transient synoptic conditions. Our event-specific analysis reveals that during ultra FC events over North America, the transient temperature gradients and meridional winds show no significant weakening trend (Supplementary Fig. 16a, c). By maintaining these sharp transient frontal structures, and occurring more frequently due to favorable circulation regime shifts, the cumulative seasonal contribution of cold advection to ultra FC occurrence robustly increases over NA. In contrast, Eurasia experiences a decline in the cumulative advection contribution, driven by a simultaneous weakening of both the transient event-scale intensity and the occurrence of favorable circulation regimes (Supplementary Fig. 16b, d).

Establishing the causal linking these circulation-regime changes to anthropogenic forcing remains a complex, open challenge. The atmospheric response to Arctic sea-ice loss is known to be strongly timescale-dependent[48]. Evidence suggests that internal variability, particularly the Arctic Oscillation, dominates Eurasian winter cooling on interannual scales, whereas Barents-Kara Sea ice loss is linked to multidecadal circulation shifts and persistent “warming-hole” over central Eurasia[49]. Additionally, cross-timescale dynamical feedbacks, where transient eddies modulate mean-flow anomalies, may contribute to Eurasian cooling as an emergent property[50]. These insights imply that FC activity reflects a superposition of internal variability, forced anthropogenic responses and eddy-mean flow feedbacks. Future research must adopt multi-timescale attribution frameworks to disentangle these compounding drivers.

Finally, the persistence and regional intensification of ultra FC events pose evolving challenges for societal adaptation. As energy systems transition toward weather-dependent renewables, they become increasingly vulnerable to rapid meteorological whiplash, where sudden cooling spikes demand, while potential icing or blocking patterns simultaneously hamper generation. Integrating rapid-cooling diagnostics into subseasonal-to-seasonal prediction frameworks is therefore urgent. Understanding whether the intensification of ultra FC events constitutes a robust new normal will be essential for designing resilient infrastructure capable of withstanding the dynamical volatility of a warming climate.

Methods

Reanalysis dataset

We utilized the ERA5 reanalysis dataset, the fifth-generation atmospheric reanalysis produced by the European Center for Medium-Range Weather Forecasts (ECMWF)[51], covering the NH winters from 1959 to 2021. ERA5 provides comprehensive surface and atmospheric fields at a native horizontal resolution of 0.25° × 0.25° and 37 pressure levels spanning 1000–1 hPa. The National Centers for Environmental Prediction (NCEP) reanalysis dataset[52] from National Center for Atmospheric Research (NCAR) was employed to cross-validate the intercontinental asymmetric trends.

For the detection of FC events, we employed daily mean 2-meter air temperature (T2m) to capture localized rapid cooling. For the thermodynamic budget analysis, we obtained hourly fields of air temperature, zonal and meridional winds, and vertical velocity. To explicitly diagnose the lower-tropospheric thermal advection while filtering out small-scale noise, we analyzed these variables at three pressure levels (825, 850, and 875 hPa) regridded to a 1° × 1° resolution. This resolution effectively resolves synoptic-scale cold surges while maintaining computationally efficiency, yielding results consistent with those derived from higher-resolution data.

To classify large-scale circulation regimes, we used daily geopotential height anomalies at 500 hPa. Prior to the SOM clustering, the geopotential height fields were regridded to a 2.5° × 2.5° resolution. This coarsening step is designed to suppress small-scale synoptic noise, thereby isolating the planetary-to-synoptic scale wave patterns that govern hemispheric teleconnections. Daily anomalies for all variables were calculated relative to the daily climatology of the 62-year study period (1959–2021), with daily mean values derived from arithmetic average of hourly data.

Identification of spatiotemporally coherent FC events

FC events were identified based on the day-to-day change in daily T2m (ΔT), a metric that effectively captures the rapid cooling characteristic of synoptic cold-air outbreaks[53]. To normalize detection across diverse climate zones and account for the spatial heterogeneity of temperature variability[24], we defined FC occurrence using a local, percentile-based threshold: $\Delta T < -1.5\sigma$ (which corresponds to approximately the $<6.68^{th}$ percentile, assuming a normal distribution), where σ is the local standard deviation of ΔT for each calendar day derived from the 1959–2021 climatology. This percentile-based approach enhances detection sensitivity in regions with high synoptic variability, such as eastern North America and northern Eurasia (Supplementary Fig. 1a). The strong spatial consistency between the identified FC frequency and the climatological variance of ΔT confirms the physical robustness of the detection strategy.

To capture the full life-cycle of these events, we implemented a 3D-connected algorithm to identify FC events as coherent volumetric structures in longitude-latitude-time space (Supplementary Fig. 17). The procedure follows a four-step sequence. First, ΔT is calculated as

the difference between T2m on consecutive days, and daily σ is computed from the 62-year ΔT climatology. Second, grid cells satisfying ΔT <−1.5σ are selected; during this step, tropical regions (T2m > 20 °C) are excluded following prior studies[16]. Third, the selected grid cells are aggregated into individual spatiotemporal objects using a 26-connected structure. This connectivity rule considers grids to be part of the same event if they share a face, edge, or corner in both space and time. Fourth, to isolate physically meaningful synoptic-scale outbreaks from transient meteorological noise (e.g., localized nighttime radiative cooling or micro-scale frontal passages), we apply a spatiotemporal filter excluding events with a duration ≤ 3 days or a projection area ≤ 10^5 km^2. These criteria represent the widely accepted conservative lower bounds established in previous literature for large-scale extreme event tracking, including cold air outbreaks[16,54], flash droughts[32,55], and continuous heatwaves[33]. To verify that our core findings are insensitive to these specific thresholds, we conducted rigorous sensitivity testing. Even under substantially stricter spatial (5×10^5 km^2 or 10^6 km^2) and temporal (≥ 4 or ≥ 5 days) constraints, the intercontinental divergence (significant intensification over NA and weakening over EA) remains robustly preserved (Supplementary Fig. 18). This cross-threshold consistency confirms that the observed divergence reflects a fundamental physical shift in the climate system, rather than a statistical artifact of the 3D-connected filtering parameters.

A critical distinction of our approach, compared to earlier applications of 3D connectivity[35] is the exclusion of a temporal overlap constraint and the adoption of the relaxed 26-connected structure (as opposed to the stricter 10-connected rules). Overlap-based constraints are optimized for quasi-stationary systems such as heatwaves or atmospheric blocking, where spatial persistence is intrinsic. In contrast, FC events are highly transient and mobile systems driven by fast-moving weather fronts, which often propagate over large distance within a single day[36,56,57]. A strict overlap or connectivity rule would artificially fracture a single rapidly propagating outbreak into multiple disconnected events. Consequently, the relaxed 26-connected structure without overlap constraints is physically better suited to the dynamical characteristics of cold surges, ensuring the continuity of their propagation pathways. Winter is defined as the boreal cold season from December 1 to February 28/29 of the following year (e.g., the 1959 winter spans from December 1, 1959, to February 28, 1960). A complete set of event-level properties for each FC event is listed in Supplementary Table 1.

Statistical methods

Linear trends were quantified using ordinary least-squares regression (OLS), with statistical significance assessed via a two-tailed Student's t-test. The Mann-Kendall test and Theil-Sen slope estimates were also applied repeatedly in key conclusive figures (Supplementary Figs. 19–22), and their consistency with the OLS results validates the robustness of the conclusions. Given the stochastic nature of rare extreme events, annual time series can be dominate by high-frequency noise. To mitigate this and enhance the signal-to-noise ratio, trend analyses (except those explicitly investigating interannual variability in Supplementary Figs. 3, 4, 6 and 13) were performed on 5-year aggregated intervals. This temporal aggregation increases the robustness of the trend detection by smoothing out transient year-to-year volatility. Furthermore, to rigorously assess the statistical significance of the intercontinental divergence ($\mathrm{Trend_{NA}}-\mathrm{Trend_{EA}}$), we employed a bootstrap resampling approach (1000 iterations) on the regional times series of ultra FC days to derive the probability density of the trend differences (Supplementary Fig. 14). This analysis reveals that alongside ERA5, the models CNRM-CM6-1 ($p < 0.05$), EC-Earth3-Veg-LR ($p < 0.1$), and MRI-ESM2-0 ($p < 0.1$) exhibit a statistically significant positive intercontinental difference. While the individual regional trend analyses establish the opposing directions of these changes (positive over NA, negative over EA, last two rows in Fig. 4a), this bootstrap resampling provides critical complementary evidence, confirming that the magnitude of this intercontinental divergence is statistically robust. Notably, these models perfectly correspond to the "ERA5-similar" circulation group, further demonstrating that successfully reproducing the observed trend divergence is fundamentally tied to accurately capturing the underlying dynamic circulation shifts.

To determine whether circulation patterns identified by the SOM are statistically significant and not an artifact of random classification, we employed a Monte Carlo randomization test. We tested the null hypothesis that the observed circulation frequency across SOM clusters could arise from a random assignment of events with equal probability to each cluster. In this procedure, the 500-hPa daily circulation fields corresponding to all ultra FC days were randomly reassigned into the 12 SOM clusters. Under the constraint that the total number of days was preserved in each iteration, this randomization procedure was repeated 100,000 times to generate a synthetic probability distribution of cluster frequencies under the null hypothesis. The 95th percentile of this distribution served as the significance threshold; a SOM cluster was deemed independent if its observed circulation frequency exceeded this threshold (Supplementary Table 2).

Applying this framework to the winter 500-hPa geopotential height anomalies yields twelve SOM nodes. When clustering was performed on all winter days, six circulation patterns (#1, #2, #4, #9, #11, and #12) satisfy the independence criterion. However, in the stricter sensitivity test trained exclusively on ultra FC days, patterns #2 and #11 over North America fell marginally below the 95$^{\mathrm{th}}$-percentile independence threshold (frequency of 8.38% and 8.13% vs. threshold of 8.94%). Despite this marginal statistical deviation, we retained these nodes for the final analysis for two physically grounded reasons. First, they remain climatologically distinct and exhibit occurrence rates well above the random expectation, indicating a non-negligible dynamical link. Second, and more importantly, the SOM preserves the topological continuity of the circulation phase space; pattern #2 and #11 represent critical transitional stages in the evolution of blocking systems. Excluding them would artificially disrupt the dynamical continuum of the cold-air outbreak lifecycle, compromising the physical interpretability of the results. Thus, all six patterns were retained to ensure a comprehensive and dynamically consistent assessment across regions.

Temperature budget and thermodynamic decomposition

To diagnose the physical drivers governing FC event variability, we performed a temperature budget analysis based on the thermodynamic equation in pressure coordinates. The local temperature tendency can be written as:

$$\frac{\partial T}{\partial t} = -u\frac{\partial T}{\partial x} - v\frac{\partial T}{\partial y} + S_p\omega + \dot{Q} + \mathrm{res} \tag{1}$$

where $\frac{\partial T}{\partial t}$ is the temperature tendency; $-u\frac{\partial T}{\partial x}$ and $-v\frac{\partial T}{\partial y}$ denote the zonal and meridional temperature advection, respectively. $S_p\omega$ represents adiabatic heating or cooling associated with vertical motion. $\dot{Q}$ denotes the diabatic heating rate, which encompasses radiative fluxes, latent heat release, and turbulent mixing; in this study, the diabatic term is calculated as:

$$\left(\frac{p}{p_0}\right)^{\frac{R}{C_p}}\left(\frac{d\theta}{dt}\right) = \left(\frac{p}{p_0}\right)^{\frac{R}{C_p}}\left(\frac{\partial\theta}{\partial t} + u\frac{\partial\theta}{\partial x} + v\frac{\partial\theta}{\partial y} + \omega\frac{\partial\theta}{\partial p}\right) \tag{2}$$

S_p can be expressed as:

$$S_p = -\left(\frac{T}{\theta}\right)\left(\frac{\partial\theta}{\partial p}\right) \tag{3}$$

where θ is the potential temperature, which can be written as:

$$\theta = T\left(\frac{p_0}{p}\right)^{\frac{R}{C_p}} \tag{4}$$

where R is the gas constant for dry air (287 J kg^{-1} K^{-1}) and C_p is the specific heat at constant pressure (1,004 J kg^{-1} K^{-1}). "res" is the residual of the budget equation. All terms in Eq. (1) are computed at 850 hPa using hourly ERA5 data.

To align the instantaneous budget with our event definition (i.e., the day-to-day temperature drop, ΔT), we perform a time-weighted integration of the hourly tendency terms. The 24-hour temperature change derived from the budget equation is expressed as:

$$\Delta T_t = T^t_{daily} - T^{t-1}_{daily} = \frac{\sum_{n=0h}^{23h} T^t_n}{24} - \frac{\sum_{n=0h}^{23h} T^{t-1}_n}{24} = \frac{\sum_{n=0h}^{23h}\left(T^t_n - T^{t-1}_n\right)}{24} \tag{5}$$

where the subscript n refers to the nth hour of the day ($0 \le n \le 23$ h). By discretizing Eq. (1), temperature changes between two days at the nth hour can be approximately calculated as:

$$\begin{aligned} T^t_n - T^{t-1}_n = &\sum_{n}^{23h}\left[\left(-u\frac{\partial T}{\partial x}\right)^{t-1}_n + \left(-v\frac{\partial T}{\partial y}\right)^{t-1}_n + \left(S_p\omega\right)^{t-1}_n + \dot{Q}^{t-1}_n\right] \\ &+ \sum_{0h}^{n-1h}\left[\left(-u\frac{\partial T}{\partial x}\right)^{t}_n + \left(-v\frac{\partial T}{\partial y}\right)^{t}_n + \left(S_p\omega\right)^{t}_n + \dot{Q}^{t}_n\right] + \mathrm{res} \end{aligned} \tag{6}$$

Substituting Eq. (6) into Eq. (5) yields:

$$\begin{aligned} \Delta T_t = &\sum_{n=0h}^{23h} w^{t-1}_n\left[\left(-u\frac{\partial T}{\partial x}\right)^{t-1}_n + \left(-v\frac{\partial T}{\partial y}\right)^{t-1}_n + \left(S_p\omega\right)^{t-1}_n + \dot{Q}^{t-1}_n\right] \\ &+ \sum_{n=0h}^{23h} w^{t}_n\left[\left(-u\frac{\partial T}{\partial x}\right)^{t}_n + \left(-v\frac{\partial T}{\partial y}\right)^{t}_n + \left(S_p\omega\right)^{t}_n + \dot{Q}^{t}_n\right] + \mathrm{res} \end{aligned} \tag{7}$$

where w_n is the weight for hour n:

$$w^{t-1}_{n=0,\,1,\,2,\,\ldots,\,23h} = \frac{1}{24}, \frac{2}{24}, \frac{3}{24}, \ldots, 1; w^{t}_{n=0,1,2,\ldots,23h} = \frac{23}{24}, \frac{22}{24}, \frac{21}{24}, \ldots, 0$$

The integration ensures that the sum of the dynamical and thermodynamical components is mathematically consistent with the ΔT metric used for event identification. Finally, to quantify the aggregate intensity of the cooling events, we defined the total cooling (TC) as the spatiotemporal integration of the temperature drop across all identified ultra FC events within a given year y:

$$\mathrm{TC}_y = \sum_{0}^{i}\sum_{t_0}^{t_0+d}\sum_k S_{k,t} * \Delta T_{k,t} \tag{8}$$

where $S_{k,t}$ is the area, and $\Delta T_{k,t}$ is the day-to-day temperature drop, for each grid (k) and day (t). Together, Eqs. (1)–(8) allow the observed 24-hour cooling to be decomposed into physical interpretable dynamical and thermodynamical components, enabling quantitative attribution of the continental-scale differences in FC behavior.

As illustrated in Fig. 2, the thermodynamic budget terms are computed as a composite across all space-time grid points comprising the identified ultra FC events within the specified domains (black boxes in Fig. 1d). To rigorously validate the reliability of this physical attribution, we quantified the thermodynamic budget closure. The mean relative closure error, defined as the ratio of the residual to the local temperature tendency, is exceptionally small, approximately −0.77% over NA and −1.68% over EA (Fig. 2c, d), confirming a tightly closed equation. Furthermore, to verify that our findings are robust to the chosen reference height, we replicated the quantitative budget analysis at 825 hPa and 875 hPa. The magnitudes of the budget terms and their long-term divergent trends are highly insensitive to the choice of pressure level (Supplementary Figs. 23 and 24). Although these pressure levels inevitably intersect surface topography in certain elevated regions, the affected areas are negligible, accounting for only 2.2%, 3.2%, and 5.3% of the total event occurrence area at 825, 850 and 875 hPa, respectively. Finally, following the method of Xie et al.[58], we evaluated the near-surface temperature budget using the second-lowest model level (Level 136). Consistent with previous studies[54], near-surface cold advection is severely weakened by boundary-layer friction and stronger diabatic cooling (Supplementary Fig.25c–f). Relying solely on near-surface temperature budget would obscure the large-scale cold advection that dynamically triggers these extreme events. Consequently, 850hPa was selected as the optimal level, striking a rigorous balance between minimizing topographic interference and accurately capturing the pristine synoptic-scale air masses.

Circulation pattern classification

To characterize the large-scale atmospheric drivers of ultra FC days, we employed the Self-organizing map (SOM) algorithm, an unsupervised neural-network-based clustering technique. Unlike discrete clustering methods (e.g., K-means) or linear decompositions (e.g., EOFs), the SOM projects high-dimensional data onto a low-dimensional lattice while explicitly preserving the topological relationships among patterns[59,60]. This feature is critical for this study, as it allows us to visualize the continuous non-linear evolution of circulation regimes, from blocking formation to decay, rather than isolating them as disjoint states.

Clustering was performed separately for the two target domains: North America (30°N–80°N, 60°W–180°W) and Eurasia (30°N–80°N, 30°E–180°E). The input feature space consisted of daily wintertime 500-hPa geopotential height (Z500) anomalies. To account for the convergence of meridians in the polar projection, anomaly fields were weighted by the cosine of latitude prior to vectorization. This ensures that clustering is driven by physical mass distribution rather than areal distortion at high latitudes.

We utilized a 4 × 3 hexagonal lattice structure with Gaussian neighborhood function, which provides six equidistant neighbors for each node, offering smoother topological transitions than a rectangular grid. The network was initialized using Principal Component Analysis (PCA) (spanning the first two eigenvectors) rather than random seeding. This deterministic initialization ensures a globally ordered map and reproducible results[61,62]. Training was conducted via the batch algorithm using the SOMPY package, consisting of a coarse ordering phase (radius=3, 50,000 iterations) followed by a fine-tuning phase (radius=2, 50,000 iterations) to minimize the quantization error[63]. The topological fidelity of the trained map was verified using Sammon mapping, which confirmed that projected 2D distance faithfully reflect the intrinsic high-dimensional structure of the circulation phase space (Supplementary Fig. 26).

The resulting SOM patterns represent the dynamical archetypes of the winter circulation (Supplementary Figs. 27 and 28). To test the sensitivity of these regimes to sampling, we compared SOMs trained on the full 63-year winter climatology against those trained exclusively on ultra FC days. The spatial correlation between the resulting reference vectors is statistically significant ($p < 0.01$), indicating that the identified patterns are robust. This congruence demonstrates that ultra FC events are not driven by atypical flow configurations, but rather by the intensification of intrinsic, recurrent modes of internal atmospheric variability.

From the 12 SOM nodes, we initially identified a robust pool of six circulation patterns with sufficient sample sizes and physical

representativeness (#1/2/4/9/11/12 in Supplementary Table 2), which collectively account for >80% of the total sample size and successfully reproduce the observed trends (Supplementary Fig. 10). From this pool, we focused our detailed mechanistic analysis on the specific nodes (#4, #11, #12 for NA; #9 for EA) that exhibit the most significant contributions to the divergent trends in ultra FC days.

Risk ratio

To quantify the dynamical modulation of ultra FC events by large-scale circulation, we calculated the Risk ratio (RR) for each grid point under each SOM-identified circulation regime. This metric standardizes the comparison across regions with heterogeneous background frequencies, allowing us to isolate the dynamical contribution of specific flow pattern[64]. The risk ratio is defined as:

$$RR = \frac{P_{cc}}{P_{hist}} \tag{9}$$

where P_{cc} denotes the conditional probability of an ultra FC day occurring at grid point given the presence of circulation cluster, and P_{hist} represents the historical climatological probability of ultra FC days at the same grid. Physically, a value of RR > 1 indicates that the specified circulation regime dynamically amplifies the local cold risk relative to the climatological baseline, whereas RR < 1 indicates suppressed risk. To ensure the reliability of these associations, statistical significance was assessed using a two-sided binomial test at the 5% confidence level. This test evaluates whether the observed frequency of ultra FC days under a given circulation differs significantly from the expected count derived from the background probability P_{hist}, thereby identifying circulation regimes that exert a statistically robust control on regional cooling extremes.

CMIP6 simulations

To evaluate the fidelity of current climate models in reproducing ultra FC dynamics, we analyzed historical simulations from 24 models participating in the Coupled Model Intercomparison Project Phase 6 (CMIP6) (Supplementary Table 3). To ensure spatial consistency with the observational baseline, daily near-surface temperature fields from each model were bilinearly interpolated to a 1° × 1° grid for identifying FC events, while daily 500-hPa geopotential height fields were interpolated to 2.5° × 2.5° resolution for circulation-pattern classification. All ERA5-based diagnostics in Fig. 4 were truncated at 2014 to align temporally with the end of the CMIP6 historical simulations (1959–2014).

A coherent assessment of model performance must account for systematic biases in the spatial location of climatic features. Compared to ERA5, the core regions of ultra FC days are substantially displaced in some models. For example, the core region of ultra FC days in models like ACCESS-CM2 exhibits a poleward shift relative to ERA5 (Supplementary Fig. 29). To ensure objective comparison across models while explicitly accounting for the spatial displacement of event hotspots, we adopted a fixed-domain averaging approach. Specifically, model-simulated ultra FC days were area-weighted and averaged over consistent continental domains: North America (40°–70°N, 70°–130°W) and Eurasia (40°–70°N, 30°–140°E). This strategy allows the evaluation to uniformly capture continental-scale signals without adjusting the analysis domain for each model, thereby reflecting biases introduced by spatial mismatches.

To strictly enforce dynamical consistency between observations and models, circulation regimes in each model were identified by projecting daily model Z500 anomaly fields onto the fixed ERA5-derived SOM patterns defined in Section 3. For each model day, the circulation state was assigned to the SOM node that minimized the Euclidean distance in pattern space. This projection approach guarantees that we are tracking the evolution of the same physical modes (e.g., the specific Alaska blocking or Ural trough configuration) across the model ensemble, rather than model-specific artifacts. Circulation frequency trends were computed as the linear changes in the occurrence of these projected nodes. Circulation intensity changes were quantified using the extreme geopotential height anomalies associated with each key pattern: the maximum anomaly within the Alaska–Arctic anticyclonic regime for North America, and the minimum anomaly within the Ural–Arctic cyclonic regime for Eurasia. This definition provides a physically robust and comparable metric of circulation amplitude change across the multi-model ensemble.

Data availability

The ERA5 single-level data used in this study are available at (https://cds.climate.copernicus.eu/datasets/reanalysis-era5-single-levels?tab=overview). The ERA5 pressure level data are available at (https://cds.climate.copernicus.eu/cdsapp#!/dataset/reanalysis-era5-pressure-levels?tab=overview). The NCEP-NCAR reanalysis data are available at (https://psl.noaa.gov/data/gridded/data.ncep.reanalysis.html). The CMIP6 historical data are available at (https://aims2.llnl.gov/search/cmip6/). The processed source data underlying the figures generated in this study are available via the Code Ocean capsule associated with this study (DOI: 10.24433/CO.9577695.v1). No restricted-access data were used in this study.

Code availability

The SOMPY library (https://github.com/sevamoo/SOMPY) was used for all SOM computations. The code used to identify and analyze flash cold events and plot figures in this work is publicly accessible at the following CodeOcean capsule: (https://doi.org/10.24433/CO.9577695.v1[65]).

References

1. Prein, A. et al. The future intensification of hourly precipitation extremes. *Nat. Clim. CHANGE* **7**, 48–52 (2017).
2. Yin, J. et al. Large increase in global storm runoff extremes driven by climate and anthropogenic changes. *Nat. Commun.* **9**, 4389 (2018).
3. Sreeparvathy, V. & Srinivas, V. V. Meteorological flash droughts risk projections based on CMIP6 climate change scenarios. *Npj Clim. Atmos. Sci.* **5**, 1–17 (2022).
4. Yuan, X. et al. A global transition to flash droughts under climate change. *Science* **380**, 187–191 (2023).
5. Lee, C. C. Weather whiplash: Trends in rapid temperature changes in a warming climate. *Int. J. Climatol.* **42**, 4214–4222 (2022).
6. Ma, S. & Zhu, C. Atmospheric circulation regime causing winter temperature whiplash events in North China. *Int. J. Climatol.* **41**, 917–933 (2021).
7. Chen, H., Jiang, J. & Liu, Y. Investigating the December 2023 warm-to-cold weather whiplash in China using a novel flash-cold metric. *Environ. Res. Lett.* **20**, 014040 (2024).
8. Liu, Q., Fu, C., Xu, Z. & Ding, A. Global warming intensifies extreme day-to-day temperature changes in mid–low latitudes. *Nat. Clim. Change* **16**, 69–76 (2025).
9. Wu, S. et al. Rapid flips between warm and cold extremes in a warming world. *Nat. Commun.* **16**, 3543 (2025).
10. Gu, L. et al. The 2007 Eastern US spring freeze: increased cold damage in a warming world? *BioScience* **58**, 253–262 (2008).
11. Ikram, M., Yan, Z., Liu, Y. & Qu, W. Seasonal effects of temperature fluctuations on air quality and respiratory disease: a study in Beijing. *Nat. Hazards* **79**, 833–853 (2015).
12. Li, H., Sun, B., Wang, H., Zhou, B. & Ma, X. Characteristics and mechanisms of the severe compound cold-wet event in southern China during February 2022. *Environ. Res. Lett.* **18**, 114021 (2023).
13. Anagnostopoulou, C., Tolika, K., Lazoglou, G. & Maheras, P. The exceptionally cold january of 2017 over the balkan peninsula: a climatological and synoptic analysis. *Atmosphere* **8**, 252 (2017).

14. Li, X., Cui, H., Chen, B., Zhang, Z. & Li, P. Discussion on reasons and mechanisms of the extreme cold waves in eastern China in January 2021 and 2024. *Coast. Eng.* **43**, 116–128 (2024).
15. National Climate Centre. Top 10 International Weather and Climate Events in 2023. *China Meteorological Administration* https://www.cma.gov.cn/en/research/news/202401/t20240122_6019177.html (2024).
16. Smith, E. T. & Sheridan, S. C. Where Do Cold Air Outbreaks Occur, and How Have They Changed Over Time? *Geophys. Res. Lett.* **47**, e2020GL086983 (2020).
17. Ribes, A., Robin, Y., Tessiot, O. & Cattiaux, J. Recent extreme cold waves are likely not to happen again this century. *Bull. Am. Meteorol. Soc.* https://doi.org/10.1175/BAMS-D-24-0013.1 (2025).
18. Cohen, J. et al. Divergent consensuses on Arctic amplification influence on midlatitude severe winter weather. *Nat. Clim. CHANGE* **10**, 20–29 (2020).
19. Francis, J. A. & Vavrus, S. J. Evidence for a wavier jet stream in response to rapid Arctic warming. *Environ. Res. Lett.* **10**, 014005 (2015).
20. Blackport, R. & Screen, J. A. Observed statistical connections overestimate the causal effects of Arctic Sea ice changes on midlatitude winter climate. *J. Clim.* **34**, 3021–3038 (2021).
21. Zhang, J., Tian, W., Chipperfield, M. P., Xie, F. & Huang, J. Persistent shift of the Arctic polar vortex towards the Eurasian continent in recent decades. *Nat. Clim. Change* **6**, 1094–1099 (2016).
22. Huang, J., Hitchcock, P., Maycock, A. C., McKenna, C. M. & Tian, W. Northern hemisphere cold air outbreaks are more likely to be severe during weak polar vortex conditions. *Commun. Earth Environ.* **2**, 1–11 (2021).
23. Li, M. & Luo, D. Winter Arctic warming and its linkage with midlatitude atmospheric circulation and associated cold extremes: The key role of meridional potential vorticity gradient. *Sci. China Earth Sci.* **62**, 1329–1339 (2019).
24. Yang, X., Zeng, G., Zhang, G. & Li, Z. Interdecadal variation of winter cold surge path in east asia and its relationship with Arctic Sea Ice. *J. Clim.* **33**, 4907–4925 (2020).
25. Mori, M., Watanabe, M., Shiogama, H., Inoue, J. & Kimoto, M. Robust Arctic sea-ice influence on the frequent Eurasian cold winters in past decades. *Nat. Geosci.* **7**, 869–873 (2014).
26. Blackport, R., Sigmond, M. & Screen, J. A. Models and observations agree on fewer and milder midlatitude cold extremes even over recent decades of rapid Arctic warming. *Sci. Adv.* **10**, eadp1346 (2024).
27. Ma, S. & Zhu, C. Extreme cold wave over East Asia in January 2016: a possible response to the larger internal atmospheric variability induced by Arctic warming. *J. Clim.* **32**, 1203–1216 (2019).
28. Park, T.-W. et al. Different characteristics of cold day and cold surge frequency over East Asia in a global warming situation. *J. Geophys. Res. Atmospheres* **116**, D12118 (2011).
29. Wang, P., Ye, F., Yang, Y., Tang, J. & Liao, H. Mitigated Rapid Temperature Variability in the Northern Mid-High Latitudes Under Carbon Neutrality. *Geophys. Res. Lett.* **52**, e2025GL118040 (2025).
30. Nie, Y., Sun, Y., Zhang, X. & Chen, G. Human-induced changes in extreme cold surges across the Northern Hemisphere. *Nat. Commun.* **16**, 8086 (2025).
31. Lv, X. et al. Characterization of the evolution of drought events in China based on 3D identification. *Arid Zone Res.* **40**, 849–962 (2023).
32. Wang, D. et al. Dynamic development of global contiguous flash droughts: from an event-based spatiotemporal perspective. *J. Hydrol.* **662**, 133934 (2025).
33. Luo, M. et al. Anthropogenic forcing has increased the risk of longer-traveling and slower-moving large contiguous heatwaves. *Sci. Adv.* **10**, eadl1598 (2024).
34. Tian, Y. et al. Characterizing heatwaves based on land surface energy budget. *Commun. Earth Environ.* **5**, 1–9 (2024).
35. He, Y., Wang, X., Zhang, B., Wang, Z. & Wang, S. Contrast responses of strong and weak winter extreme cold events in the Northern Hemisphere to global warming. *Clim. Dyn.* **61**, 4533–4550 (2023).
36. Wang, Z., Sun, Z. & Zeng, G. Characteristics of strong cold air outbreaks in China's central and eastern Mongolian region between 1970 and 2013. *Atmosphere* **8**, 98 (2017).
37. Che, J.-N. et al. Understanding the physical processes in the evolution of a cold air outbreak over China in late November 2022 from a Lagrangian perspective. *Adv. Clim. Change Res.* **14**, 681–690 (2023).
38. Liu, Z. et al. Anthropogenic intensification of Arctic anticyclonic circulation. *Sci. Adv.* **11**, eads4508 (2025).
39. Liu, J., Curry, J., Wang, H., Song, M. & Horton, R. Impact of declining Arctic sea ice on winter snowfall. *Proc. Natl. Acad. Sci. Usa.* **109**, 4074–4079 (2012).
40. Chen, H.-H. et al. Arctic warming as a potential trigger for the warm blob in the northeast Pacific. *Npj Clim. Atmos. Sci.* **8**, 1–8 (2025).
41. Li, M., Luo, D., Simmonds, I., Yao, Y. & Zhong, L. Bidimensional climatology and trends of Northern Hemisphere blocking utilizing a new detection method. *Q. J. R. Meteorol. Soc.* **149**, 1932–1952 (2023).
42. Fan, S., Chen, X. & Cohen, J. Boreal winter extratropical weather regime changes during 1979-2019 and their weather impacts and possible linkages to sea-ice in the Nordic Seas. *J. Geophys. Res. -ATMOSPHERES* **129**, e2023JD039868 (2024).
43. King, M. J., Reeder, M. J. & Jakob, C. Strong temperature falls as a cold frontal metric in Australian station observations, reanalyses and climate models. *Q. J. R. Meteorol. Soc.* **150**, 4788–4805 (2024).
44. Krauskopf, T. & Huth, R. Trends in intraseasonal temperature variability in Europe: Comparison of station data with gridded data and reanalyses. *Int. J. Climatol.* **44**, 3054–3074 (2024).
45. Shen, H. et al. Characteristics and circulation analysis of intraseasonal variability of winter temperature in China. *Meteorol. Mon.* **47**, 327–336 (2021).
46. Screen, J. A. Arctic amplification decreases temperature variance in northern mid- to high-latitudes. *Nat. Clim. Change* **4**, 577–582 (2014).
47. Blackport, R., Fyfe, J. C. & Screen, J. A. Decreasing subseasonal temperature variability in the northern extratropics attributed to human influence. *Nat. Geosci.* **14**, 719–723 (2021).
48. Cvijanovic, I. et al. Arctic sea-ice loss drives a strong regional atmospheric response over the North Pacific and North Atlantic on decadal scales. *Commun. Earth Environ.* **6**, 1–12 (2025).
49. Gong, H. et al. Teleconnection from Arctic warming suppresses long-term warming in central Eurasia. *Sci. Adv.* **11**, eadq9461 (2025).
50. Yin, M., Yang, X.-Q., Sun, L., Tao, L. & Keenlyside, N. Amplified wintertime Arctic warming causes Eurasian cooling via nonlinear feedback of suppressed synoptic eddy activities. *Sci. Adv.* **11**, eadr6336 (2025).
51. Hersbach, H. et al. The ERA5 global reanalysis. *Q. J. R. Meteorol. Soc.* **146**, 1999–2049 (2020).
52. Kalnay, E. et al. The NCEP/NCAR 40-year reanalysis project. *Bull. Am. Meteorol. Soc.* **77**, 437–472 (1996).
53. Zhang, Y., Sperber, K. R. & Boyle, J. S. Climatology and Interannual Variation of the East Asian Winter Monsoon: Results from the 1979–95 NCEP/NCAR Reanalysis. *Mon. Weather Rev.* **125**, 2605–2619 (1997).
54. Stone, J., Gervais, M., Bowley, K. A. & Zarzycki, C. Identifying, tracking, and evaluating mechanisms of North American cold air outbreaks (CAOs) using a feature tracking approach. *Mon. Weather Rev.* **153**, 153–168 (2025).

55. Herrera-Estrada, J. E. & Diffenbaugh, N. S. Landfalling droughts: global tracking of moisture deficits from the oceans onto land. *Water Resour. Res.* **56**, e2019WR026877 (2020).
56. Yang, X., Zeng, G., Zhang, G., Iyakaremye, V. & Xu, Y. Future projections of winter cold surge paths over East Asia from CMIP6 models. *Int. J. Climatol.* **41**, 1230–1245 (2021).
57. Ding, T., Gao, H. & Li, X. Increasing occurrence of extreme cold surges in North China during the recent global warming slowdown and the possible linkage to the extreme pressure rises over Siberia. *Atmos. Res.* **248**, 105198 (2021).
58. Xie, Y. et al. Changing Northern Hemisphere weather linked to warming amplification in High Mountain Asia. *Commun. Earth Environ.* **6**, 932 (2025).
59. Rousi, E., Kornhuber, K., Beobide-Arsuaga, G., Luo, F. & Coumou, D. Accelerated western European heatwave trends linked to more-persistent double jets over Eurasia. *Nat. Commun.* **13**, 3851 (2022).
60. Loikith, P., Lintner, B. & Sweeney, A. Characterizing large-scale meteorological patterns and associated temperature and precipitation extremes over the Northwestern United States using self-organizing maps. *J. Clim.* **30**, 2829–2847 (2017).
61. Francis, J., Skific, N. & Vavrus, S. Increased persistence of large-scale circulation regimes over Asia in the era of amplified Arctic warming, past and future. *Sci. Rep.* **10**, 14953 (2020).
62. Francis, J., Skific, N., Vavrus, S. & Cohen, J. Measuring 'weather whiplash' events in North America: a new large-scale regime approach. *J. Geophys. Res. -ATMOSPHERES* **127**, e2022JD036717 (2022).
63. Hewitson, B. C. & Crane, R. G. Self-organizing maps: applications to synoptic climatology. *Clim. Res.* **22**, 13–26 (2002).
64. Wu, X., Tan, X., Chen, X. & Huang, Z. Synoptic Circulation Forcing of Large-Scale Extreme Precipitation Events Over Southeastern China. *J. Geophys. Res. Atmospheres* **129**, e2024JD041396 (2024).
65. Wang, Z. & He, Y. Ultra flash cold events under global warming: codeOcean, https://doi.org/10.24433/CO.9577695.v1 (2026).

Acknowledgements

We acknowledge the Supercomputing Center of Lanzhou University for computational support.

Author contributions

Y.H., X.G. and J.H. conceived the idea for the study, and Y.H. and Z.W. conducted the analyses and drafted the manuscript. Y.H., Z.W., X.G., Y.X. and J.H. discussed the results and revised the manuscript.

Funding

Y.H. discloses support for the research of this work from the National Science Foundation of China (42595591, 42375021), the Fundamental and Interdisciplinary Disciplines Breakthrough Plan of the Ministry of Education of China (JYB2025XDXM910), Ministry of Science and Technology Gansu Province, China (25RCKA024), Central Guidance Fund for Local Science and Technology Development Projects in Gansu (24ZYQA031). J.H. discloses support for the research of this work from the National Science Foundation of China (42595591) and the Fundamental and Interdisciplinary Disciplines Breakthrough Plan of the Ministry of Education of China (JYB2025XDXM910). X.G. discloses support for the publication of this work from Ministry of Science and Technology Gansu Province, China (25RCKA024).

Competing interests

The authors declare that they have no competing interests.

Additional information

Supplementary information The online version contains supplementary material available at https://doi.org/10.1038/s41467-026-75094-6.

Correspondence and requests for materials should be addressed to Xiaodan Guan or Jianping Huang.

Peer review information *Nature Communications* thanks the anonymous reviewers for their contribution to the peer review of this work. A peer review file is available.

Reprints and permissions information is available at http://www.nature.com/reprints

Publisher's note Springer Nature remains neutral with regard to jurisdictional claims in published maps and institutional affiliations.

Open Access This article is licensed under a Creative Commons Attribution-NonCommercial-NoDerivatives 4.0 International License, which permits any non-commercial use, sharing, distribution and reproduction in any medium or format, as long as you give appropriate credit to the original author(s) and the source, provide a link to the Creative Commons licence, and indicate if you modified the licensed material. You do not have permission under this licence to share adapted material derived from this article or parts of it. The images or other third party material in this article are included in the article's Creative Commons licence, unless indicated otherwise in a credit line to the material. If material is not included in the article's Creative Commons licence and your intended use is not permitted by statutory regulation or exceeds the permitted use, you will need to obtain permission directly from the copyright holder. To view a copy of this licence, visit http://creativecommons.org/licenses/by-nc-nd/4.0/.

© The Author(s) 2026